Nanoscale

Accepted Manuscript

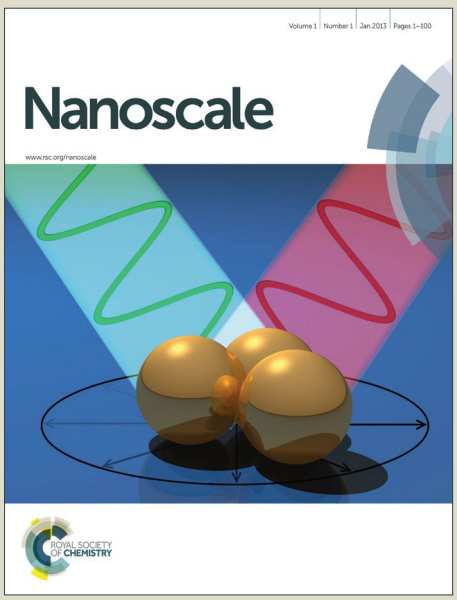

ROYAL SOCIETY OF CHEMISTRY

www.rsc.org/nanoscale

Nanoscale

PAPER

Solubility and crystallographic facet tailoring of $(GaN)_{1-x}(ZnO)_x$ pseudobinary solid-solution nanostructures as promising photocatalysts

Jing Li,[†,‡] Baodan Liu,[†,*] Wenjin Yang,[†] Yujin Cho,[§] Xinglai Zhang,[†] Benjamin Dierre,[§] Takashi Sekiguchi,[§] Aimin Wu,[‡] Xin Jiang[†,*]

Received 00th January 20xx,
Accepted 00th January 20xx

DOI: 10.1039/x0xx00000x

www.rsc.org/nanoscale

$(GaN)_{1-x}(ZnO)_x$ solid-solution nanostructures with superior crystallinity, large surface areas and visible light absorption have been regarded as promising photocatalysts for overall water splitting to produce H_2. In this work, we report the preparation of $(GaN)_{1-x}(ZnO)_x$ solid-solution nanorods with a high ZnO solubility up to 95% via a two-step synthetic routine, which starts from sol-gel reaction and follows with a nitridation process. Moreover, we clearly demonstrated that the crystallographic facets of $(GaN)_{1-x}(ZnO)_x$ solid-solution nanorods can be finely tailored from non-polar $\{10\bar{1}0\}$ to semipolar $\{10\bar{1}1\}$ and then finally to mixed $\{10\bar{1}1\}$ and polar $\{000\bar{1}\}$ by carefully controlling the growth temperature and nitridation time. Correspondingly, the ZnO content in GaN lattice can be achieved in the range of ~25% - 95%. Room-temperature cathodoluminescence (CL) measurements on the three types of $(GaN)_{1-x}(ZnO)_x$ solid-solution nanorods indicate that the minimum band-gap of 2.46 eV of the solid-solution nanorods is achieved under a ZnO solubility of 25%. The efficiency and versatility of our strategy in the band-gap and facet engineering of $(GaN)_{1-x}(ZnO)_x$ solid-solution nanorods will enhance their promising photocatalytic utilizations like an overall water splitting for H_2 production under visible-light irradiation.

Introduction

Crystal facet engineering with higher stability and less post-treatment has been regarded as an effective and promising strategy toward the optimization of surface reactivity and selectivity of nanostructures compared to conventional surface modification routines.[1, 2] The truth of this innovative strategy is that atomic configuration and coordination of different oriented crystal facets inherently govern heterogeneous surface properties which, in turn, can be utilized for gas sensing[3], ion detecting[4] and especially catalysis[5]. The synthesis and outstanding catalytic performance of series of novel metal[6] and TiO_2[5] with tailored crystal facets have inspired and guided the rapid development of a wide range of semiconductor photocatalysts such as InGaN/GaN[7], ZnO[8], SnO_2[3], $BiVO_4$[9], $SrTiO_3$[10], etc.

Recently, quaternary solid-solution nanostructures made of different binary semiconductor compounds have received significant attractions due to their peculiar optoelectronic properties and versatile functions.[11-16] As one of the most promising photocatalysts for H_2 production, $(GaN)_{1-x}(ZnO)_x$ pseudobinary solid-solution was first discovered by Madea and Domen *et al* in 2005[17] and later it was demonstrated that an overall water splitting under visible light radiation can be achieved by tailoring its band-gap.[18] The finding of $(GaN)_{1-x}(ZnO)_x$ solid solution has been considered as a significant breakthrough for visible-light-driven overall water-splitting for H_2 production and attracted worldwide attentions for their synthesis and property enhancement.[19-21] Up to date, the improvement of its catalytic activity is mainly focused on two directions: The first direction is to maximize the absorption efficiency of visible light by narrowing its band-gap. In this way, Domen and his co-workers have spent extensive efforts in the past years to narrow the band gap of $(GaN)_{1-x}(ZnO)_x$ solid solution by nitriding mixed Ga_2O_3 and ZnO powders. They found that its band gap can be tuned from 3.4 to 2.43 eV by increasing the ZnO concentration from 0 to 42% in GaN lattice due to the repulsion of N 2p and Zn 3d (O 2p) orbitals in the valence band.[17, 22] In 2010, Han *et al* further improved the ZnO solubility to 48%, which corresponds to a band gap of 2.21 eV in principle, based on a sol-gel process.[23] Later, the ZnO solubility as high as 87% was obtained and the absorption tail of $(GaN)_{1-x}(ZnO)_x$ solid solution can be extended to 600 nm through the modification and optimization of solvothermal method with nitridation processes.[21] The second direction is to modify the surface of $(GaN)_{1-x}(ZnO)_x$ solid solution with active co-catalyst, which can

[†]*Shenyang National Laboratory for Materials Science (SYNL), Institute of Metal Research (IMR), Chinese Academy of Sciences (CAS), No. 72 Wenhua Road, Shenyang 110016*, china. baodanliu@hotmail.com; xjiang@imr.ac.cn;
[‡]*School of Materials Science and Engineering, Dalian University of Technology, Dalian 116024, China*
§Nano-Electronics Materials Unit, National Institute for Materials Science (NIMS), 1-1 Namiki, Tsukuba 305-0044, Japan
Electronic Supplementary Information (ESI) available: EDS spectra, XRD patterns, diffuse reflectance spectra and SEM images of $(GaN)_{1-x}(ZnO)_x$ nanorods. See DOI: 10.1039/x0xx00000x

effectively block the recombination of photo-generated charges on the surface of catalyst. Previous research suggested that pure $(GaN)_{1-x}(ZnO)_x$ solid solution shows less photocatalytic activity in splitting water to H_2 and O_2, but the modification of co-catalyst can have an significant improvement in the photocatalytic performance of $(GaN)_{1-x}(ZnO)_x$ solid solution.[24] As a result, the overall water splitting performance of $(GaN)_{1-x}(ZnO)_x$ solid solution decorated with different co-catalysts including transition metals, metal oxides, and other core/shell or mixed metal oxides such as Ni[18], RuO_2[25], $Rh_{2-y}Cr_yO_3$[18], Rh/Cr_2O_3(core/shell)[26] etc has been fully investigated. In particular, $(GaN)_{1-x}(ZnO)_x$ powders with 18% ZnO concentration and $Rh_{2-y}Cr_yO_3$ co-catalyst can achieve an enhanced quantum efficiency as high as 5.9% for overall water splitting at a wavelength of 420-440 nm.[27]

Despite the improvements of band-gap tuning and co-catalyst reactivity, it is still too challenging to achieve commercial inner quantum efficiency (IQE) and solar energy conversion efficiency. A major limitation is that a limited amount of photo-generated carriers, which can migrate to the surface after long-way bulk diffusion process, will limit the overall efficiency of water splitting even though the decorated co-catalyst can optimize the interfacial charge transfer efficiency for $(GaN)_{1-x}(ZnO)_x$.[22] As is well-known, photo-generated electrons and holes have a high recombination rates and the crystal defects can also trap them as recombination centers.[22] Therefore, decreasing the grain size and reducing the defect concentration are considered as a potential way to increase the IQE.[28] In this way, Maeda *et al.* have demonstrated that a post-calcination process can effectively reduce the defects and improve the catalytic performance.[27] Another limitation is the surface reactivity which is strongly related to different facets and surface atomic structures like dopants and defects. Clearly, an efficient photocatalysis process requires the effective absorption of reactant molecules/ions (*i.e.*, water, CO_2, organic compounds) on the photocatalyst surface before surface electrons transfer. Previous research demonstrated that the different facets could exhibit distinct absorption abilities.[5] For instance, the (001) facet of anatase TiO_2 allows the dissociation of water, while the (101) surface can only realize the absorption of water molecular.[29] The dissociation of water is beneficial to the water splitting and the photo-decomposition of organic pollutants. Han *et al.* verified that an enhanced photo-degradation of methylene blue can be achieved by increasing the percentage of anatase {001} facets.[30] The high production of hydrogen was obtained for the anatase TiO_2 with 14.9% {001} area compared to 85.1% {101}.[31] Therefore, the facet tailoring of $(GaN)_{1-x}(ZnO)_x$ solid-solution would be of great importance and potential to pave a solid way for promoting the water splitting. However, little attention has been paid to this field.

In this work, we intend to tune the crystallographic facets and band-gap of $(GaN)_{1-x}(ZnO)_x$ solid solution nanostructures for the future optimized water splitting performance under visible irradiation. Based on the synthesis routines designed by our group for pseudobinary GaP-ZnS[32] and GaP-ZnSe[33] solid solution nanowires, three groups of representative $(GaN)_{1-x}(ZnO)_x$ nanorods with tunable crystallographic facets and different ZnO solubilities are successfully prepared by means of a sol-gel method with follow-up nitridation processes. Meanwhile, the crystallographic facet evolution mechanism of $(GaN)_{1-x}(ZnO)_x$ solid solution as a dependence of ZnO concentration (or nitridation process) is systemically discussed and the optical properties of $(GaN)_{1-x}(ZnO)_x$ solid solution nanorods with different ZnO solubilities are investigated using spatially-resolved cathodoluminescence (CL).

Results and discussion

Structural and chemical analyses

Structurally, since wurtzite(WZ) GaN and ZnO feature the same hexagonal structures and possess very close lattice constants (Fig. 1a), it is principally feasible to achieve $(GaN)_{1-x}(ZnO)_x$

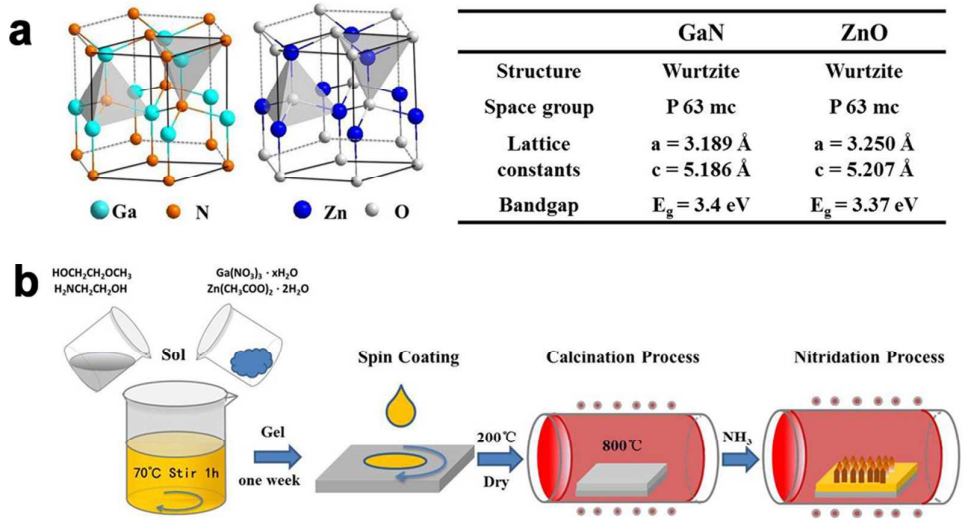

	GaN	ZnO
Structure	Wurtzite	Wurtzite
Space group	P 63 mc	P 63 mc
Lattice constants	a = 3.189 Å c = 5.186 Å	a = 3.250 Å c = 5.207 Å
Bandgap	E_g = 3.4 eV	E_g = 3.37 eV

Fig. 1. (a) Crystal structure models and parameters of wurtzite GaN and ZnO. (b) schematic diagram depicting the preparation process of $(GaN)_{1-x}(ZnO)_x$ solid-solution nanostructures;

solid-solution nanostructures with a tunable solubility according to the formation rule of pseudobinary solid-solution proposed in our previous work.[32, 33] Unfortunately, previous works demonstrated that it is quite challenging to dope high concentration of ZnO into GaN host lattice in spite of the use of Au catalyst in a traditional chemical vapor deposition (CVD) process.[32] The main problem responsible for the lower ZnO content comes from the fact that a higher reaction temperature will evaporate the Zn from the GaN lattice. To overcome this problem, an in-situ growth strategy on the precursor film at a medium temperature is in turn proceeded. Fig. 1b presents the synthetic routines of final $(GaN)_{1-x}(ZnO)_x$ solid-solution nanostructures. In a typical process, Ga-Zn-O film precursors are first prepared by a sol-gel method and subsequent calcinations to provide Ga, Zn and O sources. Following this step, a nitridation process of the precursor film at a medium temperature is conducted to obtain the $(GaN)_{1-x}(ZnO)_x$ solid-solution nanostructures.

Fig. 2a, 2e and 2i shows the representative SEM images of $(GaN)_{1-x}(ZnO)_x$ nanorods with different surface morphology and their corresponding schematic crystal models, indicating an obvious evolution in crystal facets. Typically, hexagonal nanorods surrounded by six smooth side walls and a pyramid tip can be observed in Fig. 2a. The six crystallographic planes parallel to the growth direction can be further identified to the symmetrical 6-fold $\{10\bar{1}0\}$ facets, according to the lattice fringe distance of 0.28 nm (revealed by HRTEM image in Fig. 2c) which approaches well to the theoretical value 0.281 nm of $\{10\bar{1}0\}$ facets in WZ-ZnO. The c-axis growth direction of $(GaN)_{1-x}(ZnO)_x$ nanorods is evidenced by the lattice fringes with a d-spacing of 0.52 nm (Fig. 2c) and the strong peak intensity of (0001) plane from the X-ray diffraction (XRD) pattern (Fig. S2). The angle measurement between the projected edge and the base plane of the nanorod (Fig. 2b and 2c) gives rise to a value of ~61.5°, implying that the side planes in the top pyramid are equivalent $\{10\bar{1}1\}$. The regular HRTEM fringes and selected area electron diffraction (SAED) patterns (Fig. 2c-2d), taken along the $[2\,\bar{1}\,\bar{1}\,0]$ zone axis, clearly demonstrate the single crystal characteristic of the nanorod with a WZ-type structure. The possibility of phase separation of GaN and ZnO, which have quite close lattice constants (Fig. 1a), can be excluded from the sole diffraction peaks of ZnO except to $ZnGa_2O_4$ in XRD pattern (Fig. S2). According to the X-ray energy dispersive spectrum (EDS) results shown in Fig. 3c , the $(GaN)_{1-x}(ZnO)_x$ nanorods synthesized at 800°C for 30 min have all the elements of Ga, Zn, N and O with a predominant ZnO concentration of ~95% (calculated from the EDS data shown in Fig. S1b), suggesting a ZnO host lattice with GaN

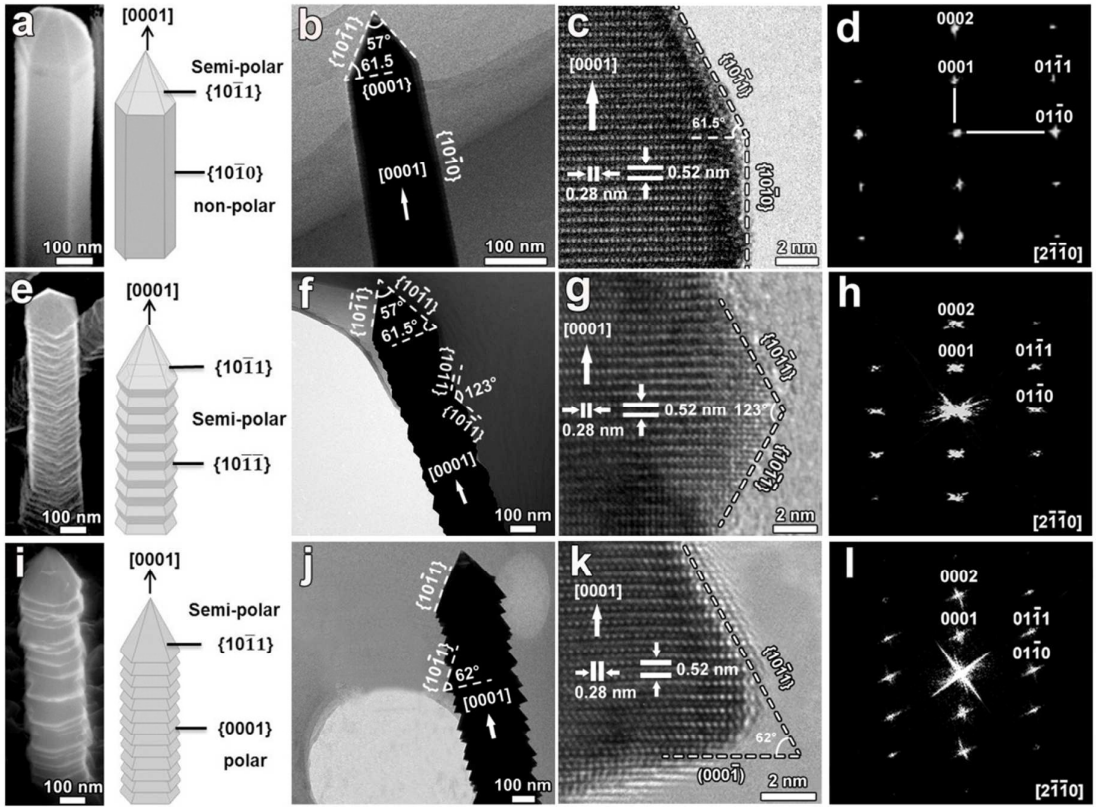

Fig. 2. Morphology and atomic structure of three typical $(GaN)_{1-x}(ZnO)_x$ solid-solution nanorods. (a, e, i) SEM images and schematic of three WZ $(GaN)_{1-x}(ZnO)_x$ nanorods (representative growth time: 30, 60 and 120 min at 800°C) with different percentages of $\{10\bar{1}0\}$, $\{10\bar{1}1\}$ and $\{000\bar{1}\}$ facets. (b, f, j) bright-field TEM images of three typical $(GaN)_{1-x}(ZnO)_x$ nanorods. (c, g, k) HRTEM images recorded from corresponding nanorods with c-axis orientation. (d) SAED and (h, l) Fast Fourier Transformation (FFT) patterns from the corresponding HRTEM images shown in c, g, k.

dopants. To clarify the spatial distribution of the four elements in $(GaN)_{1-x}(ZnO)_x$ nanorods, EDS analysis paired with spectrum imaging and line-scanning functions in scanning transmission electron microscopy (STEM) mode is carried out.[32] The corresponding elemental maps of Ga, Zn, N and O (displayed in Fig. 3a) clearly reveal that each element has a uniform spatial distribution inside the nanorod. Besides, it can be seen that Zn map has a higher intensity than Ga map, confirming the predominant content of ZnO in the solid-solution nanorods. The elemental line-scan curves along the radial direction (Fig. 3b) show up a plat-like distribution in the center of nanorods which can be attributed to the hexagonal geometrical profile of nanorods (Fig. S4a).

Compared to pyramid-like columns with dominant exposed $\{10\bar{1}0\}$ facets, we also prepare another morphological $(GaN)_{1-x}(ZnO)_x$ solid-solution nanorods with all exposed $\{10\bar{1}1\}$ facets by extending the nitridation time to 60 min. Detailed morphology and crystal structure can be seen in Fig. 2e-2h. In Fig. 2e, one can see that the nanorods exhibit a distinct appearance with the one shown in Fig. 2a and have a corrugated surface morphology, as observed in the GaN nanorods grown on graphite.[34] From the corresponding bright-field TEM image shown in Fig. 2f, the projected planes of edge surfaces are either parallel to each other or have a fixed angle. The angle between neighboring surfaces is roughly measured to be 123° (as marked in Fig. 2f and 2g), which is quite close to the value of 123.2° or 123.9° between $\{10\bar{1}1\}$ and $\{10\bar{1}\bar{1}\}$ facets in WZ-ZnO and WZ-GaN, respectively. In addition, the clear lattice fringes with a d-spacing of 0.52 nm are also observed along the long-axis direction in HRTEM image (Fig. 2g), indicating the good crystal quality and the c-axis oriented growth. Similar to the $\{10\bar{1}0\}$ faceted nanorods, the $\{10\bar{1}1\}$ faceted $(GaN)_{1-x}(ZnO)_x$ nanorods also show an obvious characteristic of solid-solution, as convinced by the composition-related measurements presented in Fig. 3d-f. The elemental maps and line-scan curves of Ga, Zn, N and O elements demonstrate a uniform spatially-resolved distribution of each element and the richer ZnO concentration (~80%, calculated from EDS data and listed in Fig. S1b) within the nanorods.

Further extending the reaction time to 120 min leads to the formation of $(GaN)_{1-x}(ZnO)_x$ solid-solution nanorods with tower-like morphology, as shown in Fig. 2i. Compared to the nanorods with corrugated morphology surface (Fig. 2d), the projected planes of the nanorod edges including pyramid tips in Fig 2j are all parallel to

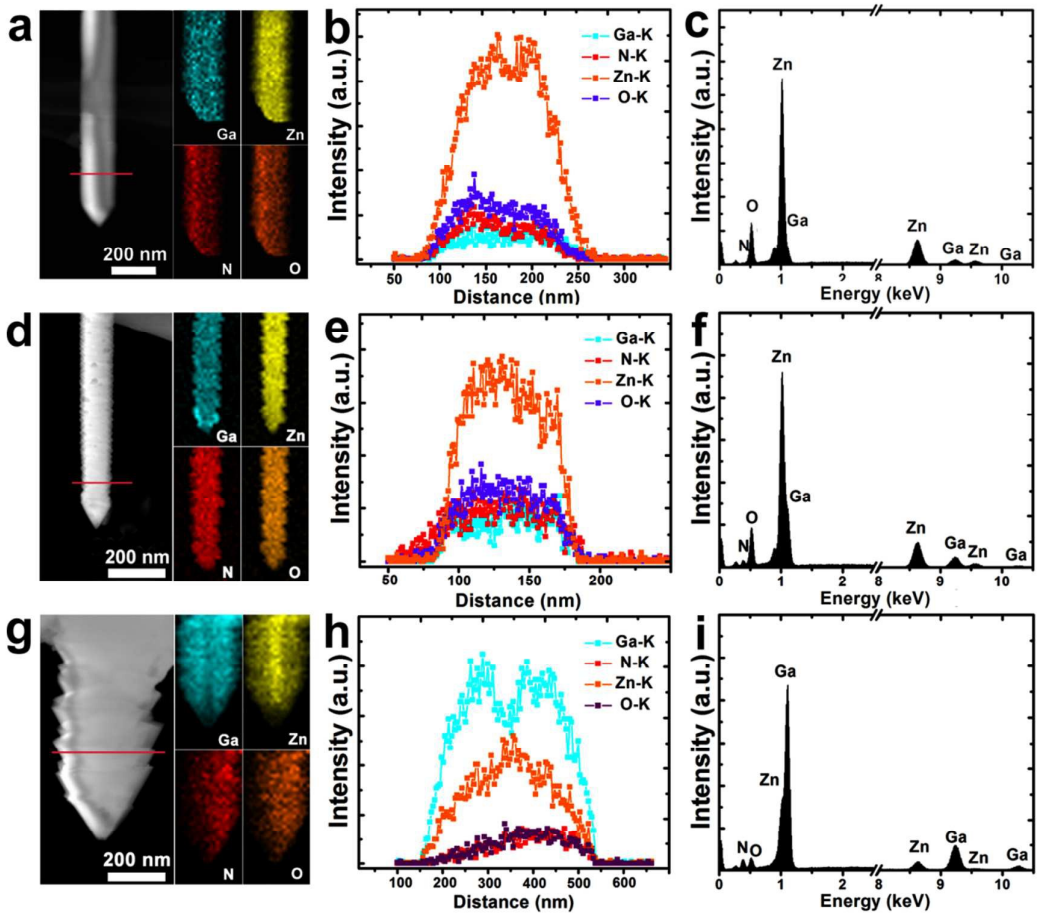

Fig. 3. (a, d, g) STEM images and corresponding elemental maps of three typical $(GaN)_{1-x}(ZnO)_x$ solid-solution nanorods (30, 60 and 120 min). (b, e, h) Elemental profiles of $(GaN)_{1-x}(ZnO)_x$ nanorods taken along the radial direction. (c, f, i) EDS spectra of $(GaN)_{1-x}(ZnO)_x$ nanorods at different growth time: 30, 60 and 120 min.

each other, which looks like the stacking of numerous hexagonal pyramids along the growth direction. Interestingly, the nanorods show exposed facets of $\{10\bar{1}1\}$ and $\{000\bar{1}\}$ planes, which can be confirmed by the measured angle of 62° and the d-spacing of fringes with a distance of 0.52 nm. Meanwhile, the clear lattice fringes and the sole diffraction pattern in Fig. 2k and 2l also illustrate that the as-synthesized $(GaN)_{1-x}(ZnO)_x$ solid-solution nanorods are perfect single crystal. Based on the peak disappearance of $ZnGa_2O_4$ phase in the XRD pattern and the good peak matching with that of WZ-GaN (Fig. S2), a conversion of the host lattice from ZnO to GaN with the prolonging of nitridation time can be confirmed. As shown in Fig. 3f and Fig. S1b, such $(GaN)_{1-x}(ZnO)_x$ solid-solution nanorods have a predominant composition of GaN as high as ~75% (calculated from EDS data). However, it shows a totally different distribution of elements compared to the above two $(GaN)_{1-x}(ZnO)_x$ solid-solution nanorods with exposed facets $\{10\bar{1}0\}$ and $\{10\bar{1}1\}$, according to the elemental mapping and the line-scan results in Fig. 3g-h. The Ga element shows obvious gradient distribution along the radial direction, with respect to the rich distribution of Zn element in the center. In particular, the cross-section image of broken (Fig S4c) nanorods clearly demonstrates the hollow characteristic of the nanorod. Based on the gradient decrease of ZnO concentration (Fig. S1b) and the appearance of local Ga aggregation on the top of $(GaN)_{1-x}(ZnO)_x$ nanorod surface (Fig. 3d), the Kirkendall Effect can be used to explain the solid diffusion process and composition difference, as observed in Co_3S_4 and CoO hollow spheres.[35] Due to the intense instability and strong volatility of ZnO phase, it is supposed that the diffusion rate of Zn and O atoms from the inner core to the outer surface is much faster than that of Ga and N atoms from the surface to the inner part, which will in turn cause the core of nanorods gradually being "eaten" and the appearance of ZnO composition gradient. Similar solid diffusion process has been observed in the formation of $(GaN)_{1-x}(ZnO)_x$ solid-solution nanotubes, in which GaN/ZnO core-shell heterostructures are used as a precursor template at high temperature.[36] As a result, it can be concluded that the last typical nanorods are actually $(GaN)_{1-x}(ZnO)_x$ nanotubes with exposed facets $\{10\bar{1}1\}$ and $\{000\bar{1}\}$.

Facets and composition tuning

As mentioned above, we have prepared three typical $(GaN)_{1-x}(ZnO)_x$ solid-solution nanostructures with different percentage of $\{10\bar{1}0\}$, $\{10\bar{1}1\}$, $\{000\bar{1}\}$ facets by controlling the nitridation process. It should be noted that the appearance of different crystallographic facets is mainly realized by tailoring of ZnO solubility. In particular, the reaction temperature and growth time are two important factors responsible for the feasible crystallographic facet engineering. The low-magnification SEM images in Fig. 4a-4c show that an optimized reaction temperature of 800 °C favors the growth of $(GaN)_{1-x}(ZnO)_x$ solid-solution nanorods with a high aspect ratio. It can be observed that the nanorods with rough morphology, an average diameter of 200 nm and a length up to 2 μm (Fig. 4a) grow from the Zn-Ga-O precursor film at 800 °C for 60 min. Corresponding composition measurements in TEM demonstrate that the nanorods have all elements of Ga, Zn, N and O with a maximum ZnO composition of ~80%, which is higher than 70% in SEM mode due to the extra signal interference from films (shown in Fig. S1b). When the temperature is increased to 850°C and 900°C, the surface morphology and the size of $(GaN)_{1-x}(ZnO)_x$ solid-solution nanorods exhibit an increasing tendency in roughness and diameter (see inset images in Fig. 4b and 4c). Consequently, the ZnO composition decreases dramatically (Fig. S1a), suggesting a rapid radial growth and high instability of ZnO under higher temperature.

The influence of reaction time on the crystallographic facet transformation is also further investigated. Obviously, the nanorods grown at 800 °C for 30, 60 and 120 min (Fig. 4d - 4f) exhibit distinct crystallographic geometries as a dependence of reaction time. In Fig. 4d, the as-prepared $(GaN)_{1-x}(ZnO)_x$ solid-solution nanorods show a regular hexagonal feature on side walls and the pyramid tip. When the reaction time is increased to 60 min, the $(GaN)_{1-x}(ZnO)_x$ solid-solution nanorods show less change in diameter (150-300 nm) and length (~2 μm) with those of 30 min. However, a significant morphology difference is observed on magnified SEM image (the inset image of Fig. 4e). The smooth side surface of $(GaN)_{1-x}(ZnO)_x$ solid-solution grown with 30 min becomes rather rough and shows a corrugated appearance. Similar geometrical shape of GaN nanostructures has been reported in previous studies.[34] Further extending the reaction time to 120 min leads to the dramatic increase of the nanorod diameter to ~600 nm and an obvious morphology evolution to hexagonal pyramids linked along the c-axis (Fig. 4f) is observed. According to the structural and chemical analysis in Fig. 2 and Fig. 3, three typical nanostructures under different growth time have been identified as $(GaN)_{1-x}(ZnO)_x$ solid solution with different percentage of $\{10\bar{1}0\}$, $\{10\bar{1}1\}$, $\{000\bar{1}\}$ facets. In the case of 30-min reaction, the nanorods are mainly surrounded by 6-fold symmetrical $\{10\bar{1}0\}$ facets and the ZnO concentration can be up to ~95%. Increasing the reaction time to 60 min induces the exposure of $\{10\bar{1}1\}$ facets and correspondingly the content of ZnO decreases to ~80%. Further extending of the reaction time to 120 min directly leads to the disappearance of some $\{10\bar{1}1\}$ facets and the formation of $\{000\bar{1}\}$ facets. As a result, the content of ZnO is minimized to about 25%. From the crystallographic structure of GaN and ZnO shown in Fig. 1a, we can see that tetrahedrally coordinated Ga(Zn)

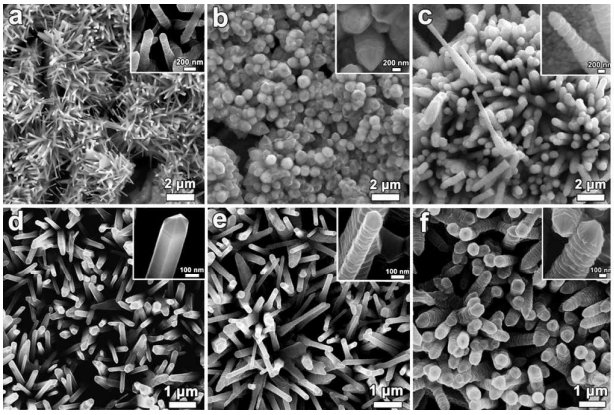

Fig. 4. (a-c) SEM images of $(GaN)_{1-x}(ZnO)_x$ nanorods at different growth temperatures (respectively: 800 °C, 850 °C, 900 °C) for 60 min. (d-f) SEM images of $(GaN)_{1-x}(ZnO)_x$ nanorods at 800 °C for different growth time: 30, 60, and 120 min. The insets show the high-magnification SEM images.

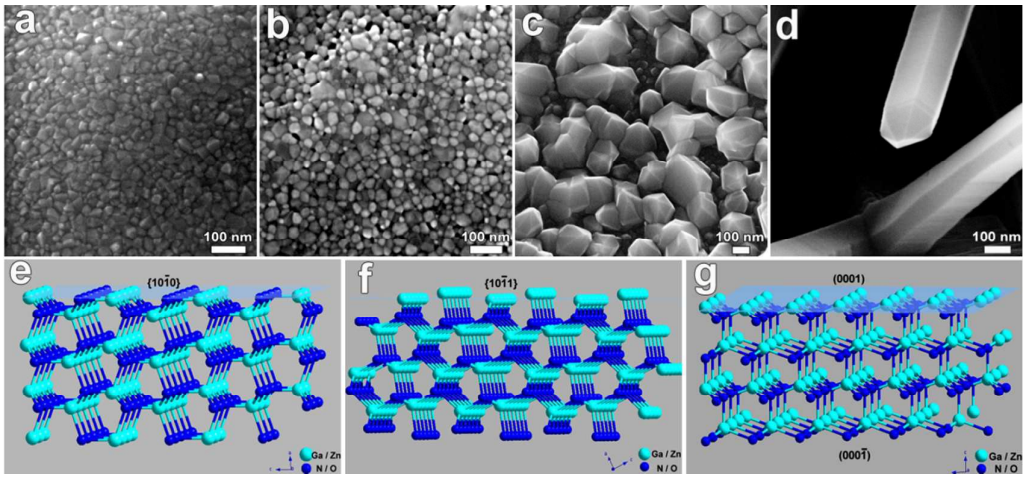

Fig. 5. Time dependent synthetic experiments to clarify the growth mechanism of $(GaN)_{1-x}(ZnO)_x$ nanorods. (a-d) High magnification SEM images of precursor film surface morphology under different growth time (respectively: 1 min, 5 min, 10 min, 30 min) at 800 °C. (e-f) schematic model of non-polar {10$\bar{1}$0}, semi-polar {10$\bar{1}$1} and polar {000$\bar{1}$} facets with different termination.

and N(O) atoms inside a WZ structure are alternately stacked along the c-axis. Such structure feature results in a spontaneous polarization of the {0001} surface and a divergence in surface energy. Since the formation of $(GaN)_{1-x}(ZnO)_x$ pseudobinary solid solution can be regarded as a simultaneous co-doping process, in which the Ga(N) atoms randomly substitute corresponding Zn(O) atoms, the polarization of $(GaN)_{1-x}(ZnO)_x$ solid-solution would still keep consistent with GaN or ZnO. Therefore, compared with the high-energy of polar {0001} surfaces, the non-polar {10$\bar{1}$0} surfaces exhibit the lowest surface energy and the semi-polar {10$\bar{1}$1} facets possess a middle surface energy.[37] Hence, it is worthwhile to study the reactivity and selectivity of these different facets to optimize the overall water splitting performance.

Composition tuning of $(GaN)_{1-x}(ZnO)_x$ solid-solution nanorods is closely related to the band-gap narrowing, i.e. harvesting more visible light for an enhanced water-splitting performance for H_2 production.[17] Based on the innovating strategy proposed and tested in this work, the solubility of ZnO in a wide range of 25% - 95 % (Fig. S1b) can be selectively tuned by controlling the growth temperature and reaction time. In addition, the similar tendency of composition variation in the solid-solution nanorods, for instance, the monotonic increase of Ga(N) or decrease of Zn(O) as a dependence of nitridation temperature (Fig. S1b), indicates that a co-doping process is indeed involved in the formation of pseudobinary $(GaN)_{1-x}(ZnO)_x$ solid solution.[32, 33] From the UV-visible diffuse reflectance spectra shown in Fig. S3, it can be seen that the absorption edge of $(GaN)_{1-x}(ZnO)_x$ solid-solution nanorod shifts to the visible light region after nitridaiton, suggesting an obvious band gap shrinking by the alloying of GaN and ZnO.[17, 21] Particularly, the absorption tail of 60-min sample can be even extended to the yellow range (about 500 nm). Interestingly, an additional strong absorption band beyond 375 nm up to the red range is also observed in 30-min sample. This absorption band can be assigned to the presence of oxygen and nitrogen vacancies in the precursor film, as observed TiO_2,[38] due to the high volatilization of ZnO and the incomplete nitridation. Its gradual disappearance as the increase of growth time further justifies our explanation. It should be noted the UV-vis absorption spectra are collected from both the nanorods and the underneath films, so it is quite difficult to disclose the exact relationship between the band-gap tailoring and the composition in nanorods, and it still requires some other high-resolution measuring techniques like CL.[39]

Mechanisms of nanorods growth and facets tuning

The initial nucleation plays a key role in guiding the growth and morphology evolution of $(GaN)_{1-x}(ZnO)_x$ solid-solution nanorods with high ZnO concentration. To clarify their nucleation and crystallization process, series of time-dependent growth experiments are carried out. At the first 1-min, the Zn-Ga-O precursor film surface is totally covered with some irregular nanoparticles with an average size of ~ 10 nm (Fig. 5a). Increasing the growth time to 5 minutes will lead to the fast growth of crystal grains to a larger size (Fig. 5b) and a growth of 10 min brings to the appearance of hexagonal pyramids with regular crystal facets (Fig. 5c). Based on the morphology transformation of the precursor film surface under different nitridation processes, it can be surmised that the nucleation process of $(GaN)_{1-x}(ZnO)_x$ solid-solution nanorods can be defined as Ostwald ripening.[40]

Why do the {10$\bar{1}$0}, {10$\bar{1}$1} and {000$\bar{1}$} facets define the stable shape of $(GaN)_{1-x}(ZnO)_x$ nanostructures during their growth? It is found that the growth time is not the key factor to govern the crystal facets because similar morphology of the $(GaN)_{1-x}(ZnO)_x$ nanorods can also be obtained under different growth temperatures (Fig. 4). Based on the significant difference of ZnO concentration (Fig. S1b) in these three samples, it is speculated that the ZnO solubility may directly influence the crystal facets evolution of $(GaN)_{1-x}(ZnO)_x$ solid-solution nanorods. In the initial nucleation, the Zn/O concentrations in the vapor is much higher than that of Ga/N atoms due to the high volatilization of ZnO in spite of the higher percentage of Ga atoms (Zn : Ga = ~ 2 : 3) in the initial sol-gel film. As a result, a large percent of Zn and O atoms will be absorbed on the nucleation surface to facilitate the growth of $(GaN)_{1-x}(ZnO)_x$

nanorods. Based on the Gibbs-Wulff Law[41] in crystal growth, which dominates in thermodynamics, the surface energy minimization is the direct drive to determine the equilibrium morphology of nano-materials due to their high surface area. As a result, the $(GaN)_{1-x}(ZnO)_x$ nanorods are mainly surrounded by six smooth non-polar $\{10\bar{1}0\}$ facets with the lowest surface energy and the ZnO concentration can be up to 95% at 30-min growth. As for the nanorods with all semi-polar $\{10\bar{1}1\}$ facets exposed, it is quite difficult to obtain only under the thermodynamic equilibrium conditions due to a fast growth rate and a high surface energy. However, this can be reasonably explained if the growth kinetics becomes predominant in the later growth stage in comparison with the thermodynamics. Increase of the growth time to 60 min will lead to the drastic decrease of ZnO concentration in the sol-gel precursor film, which in turn increases the Ga/N contents in vapor. This change in reaction vapor will create an additional barrier for the axial-growth of $(GaN)_{1-x}(ZnO)_x$ nanorods. Meanwhile, the etching from H▪ against to Zn and O cannot be ignored due to its low absorption concentration on the nanorod surface. This means that a competition between the etching and growing of the crystal facets exists in the later growth stage, which will govern the net growth rate of corresponding crystal facets. For instance, the $\{10\bar{1}1\}$ facets with higher surface energy theoretically have a faster growth rate than that of $\{10\bar{1}0\}$ facets. However, the $\{10\bar{1}1\}$ facets are easily etched by H▪ groups at high temperature due to the termination of Zn and Ga atoms (O and N atoms) on the planes (Fig. 5f). As a result, the net growth rate of $\{10\bar{1}1\}$ facets is still lower than that of $\{10\bar{1}0\}$ facets. Based on the crystal growth kinetics, the final crystallographic geometry is mainly determined by the facet with lowest growth rate. Therefore, it can be found that $(GaN)_{1-x}(ZnO)_x$ solid-solution nanorods grown under 60-min have similar size to the sample with 30-min growth, but possess a rather rough morphology surface with $\{10\bar{1}1\}$ facets.

As the growth temperature or reaction time increases, the ZnO composition in the film and nanorods exhibits a significant decrease, while the GaN content in the nanorods gradually increases to a high value. It can also be seen in Fig. 4f that the nanorods have a fast radial growth rather than the axis direction. That is because that the richness of ZnO in the center of nanorods (Fig.3) can be an additional energy barrier for axial growth compared to radial growth. As to the appearance of polar $\{000\bar{1}\}$ facets, the most reasonable illustration is that under the given conditions, they have relatively lower growth rates in contrast to other low index facets. According to the schematic model in Fig. 5g, the $\{000\bar{1}\}$ facets show the similar N, O-terminated polarity with $\{10\bar{1}\bar{1}\}$ facets. Hence, it can be concluded that the exposed facets are Ga, Zn-terminated $\{10\bar{1}1\}$ and N, O-terminated $\{000\bar{1}\}$ under 120 min growth. The evolution of $\{000\,\bar{1}\}$ from N, O-terminated $\{10\,\bar{1}\bar{1}\}$ may arise from the oxygen-deficient conditions, which is mainly due to the consumption of the residual oxygen in the Zn-Ga-O precursor film and reaction chamber. In addition, the N, O-terminated $\{000\,\bar{1}\}$ plane is close-packed and owns higher surface energy compared to $\{10\bar{1}\bar{1}\}$ facets. Under such poor oxygen conditions, the $\{000\bar{1}\}$ facets will have a lower growth rate than that of N, O-terminated $\{10\bar{1}\bar{1}\}$ facets. It should be noted that the appearance of all the exposed crystallographic planes with low index facets follows the rule of surface energy minimization.

Optical properties

$(GaN)_{1-x}(ZnO)_x$ solid solution with tunable band-gap and efficient visible light absorption has been regarded as a promising photocatalyst for visible-light-driven overall water splitting.[17] Hence, it is worthwhile to precisely study the band-gap variation depending on the ZnO solubility and to explore a suitable band-gap for optimized performance of water splitting under visible light irradiation. Previous research works using UV-vis spectrometer technique (low resolution) demonstrated that the band-gap of $(GaN)_{1-x}(ZnO)_x$ solid-solution is always decreasing with the

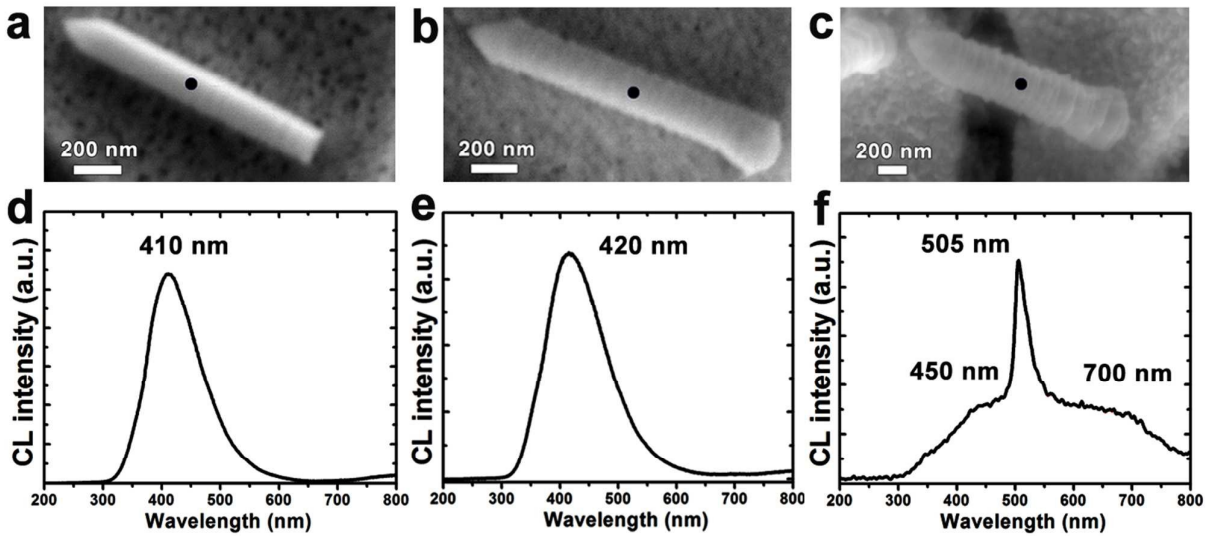

Fig. 6. (a-c) SEM images and (d-f) in-situ CL spectra of single $(GaN)_{1-x}(ZnO)_x$ nanorod grown at different growth time: 30 min, 60 min and 120 min.

continuous increase of ZnO concentration to 87%.[21] However, theory calculation has predicted that the band gap of $(GaN)_{1-x}(ZnO)_x$ solid-solution would have a minimum value of 2.29 eV for an intermediate ZnO concentration with x=0.525.[42] Therefore, it is still essential to accurately assess the band-gap change as a dependence of ZnO concentration, especially in nanoscaled $(GaN)_{1-x}(ZnO)_x$ solid-solution. For this purpose, high-resolution CL is used to characterize the as-synthesized three typical $(GaN)_{1-x}(ZnO)_x$ nanostructures at different growth time of 30, 60 and 120 min in this work. According to the CL spectra of $(GaN)_{1-x}(ZnO)_x$ solid-solution nanorods for 30 min (Fig. 6d), one can see that the near band edge emission (NBE) peak of ZnO (368 nm / 3.37 eV) or GaN (365 nm / 3.4 eV) has disappeared and instead a single peak of 410 nm (3.02 eV) with a broad range of 300 nm shows up due to the formation of $(GaN)_{1-x}(ZnO)_x$ solid solution. Interestingly, the nanorods at a growth time of 30 min have a higher ZnO solubility of 95 % (Fig. S1b). Increasing the reaction time to 60 min, the CL peak emission wavelength of the $(GaN)_{1-x}(ZnO)_x$ nanorod has a slight red-shift to 420 nm (2.95 eV), which corresponds to a ZnO concentration of 80%. As to the nanotubes with exposed $\{10\bar{1}1\}$ and $\{000\bar{1}\}$ facets at a growth time of 120 min, the CL spectra have a completely different feature with that of 30-min and 60-min samples. As shown in Fig. 6f, three peaks separately at 450, 505 and 700 nm show up in the range of 200-800 nm. The strong luminescence peak at 505 nm can be attributed to the deep-level emissions from the nanotube surface section with GaN rich, while the weak shoulder at 450 nm arises from the hollow section rich in ZnO, which is verified by EDS mapping and line-scan analysis in Fig 3g. Besides, another weak shoulder peak at 700 nm can also be observed, which is generally regarded as a result of some impurity-induced or defect-related energy levels.[34] It should be noted that this red band (700 nm) is not observed in above high ZnO concentration samples. Considering the formation of N and O terminated $\{000\bar{1}\}$ and the growth condition of oxygen-poor atmosphere, O vacancies from the nanotube surface may be mainly responsible for the red band emission.

Consequently, three typical nanostructures of $(GaN)_{1-x}(ZnO)_x$ with corresponding ZnO concentration of 95%, 80% and 25% are investigated to have lower band-gaps of 3.02 eV, 2.95 eV and 2.46 eV by room-temperature cathodoluminescence measurements. The mechanism of band-gap lowering can be attributed to the repulsion of N 2p and Zn 3d orbits owing to the alloying of GaN and ZnO, which is widely accepted under intense debates.[17, 42] As the band-gap tailoring of $(GaN)_{1-x}(ZnO)_x$ solid-solution nanorods, together with the crystallographic facet tuning, can be feasibly realized through the control of ZnO solubility in our proposed strategy, an improved photocatalytic performance in overall water splitting for H_2 production, as well as other related photocatalytic application in energy harvesting and environmental photodegradation can be expected.

Conclusions

In summary, series of $(GaN)_{1-x}(ZnO)_x$ nanostructures with controllable crystallographic facets and tunable solubilities have been obtained by means of a sol-gel method combined with nitridation processes. Using HRTEM, we clearly demonstrate that the crystallographic facets of $(GaN)_{1-x}(ZnO)_x$ solid solution nanorods can be finely tuned from non-polar $\{10\bar{1}0\}$ to semi-polar $\{10\bar{1}1\}$and then polar $\{000\bar{1}\}$ by simply controlling the growth temperature and nitridation time. Meanwhile, the band-gap of $(GaN)_{1-x}(ZnO)_x$ solid-solution nanorods can be selectively tailored in the range of 2.46-3.02 eV by altering the ZnO content from 25% to 95%, enabling an enhanced visible light absorption. The successful synthesis of $(GaN)_{1-x}(ZnO)_x$ solid solution nanostructures with controllable crystallographic facets and tunable ZnO composition will undoubtedly pave a solid way for promoting their applications in overall water splitting for H_2 production and environmental issue.

Experimental section

Synthesis of $(GaN)_{1-x}(ZnO)_x$ nanorods

$(GaN)_{1-x}(ZnO)_x$ nanostructures were synthesized by a simple method of sol-gel followed by a nitridation process, as shown in Fig. 1. Firstly, gallium nitrate hydrate (6.71 g) and zinc acetate dihydrate (2.47 g) were mixed in the solution of ethanolamine (2.3 mL) and 2-methoxyethanol to form a transparent sol (50 mL) at 70 °C for 60 minutes. Then, the sol was coated on a cleaned silicon wafer ([100]-orientation) and dried to gel at 200 °C for 15 minutes. After a calcination at 800 °C for 60 minutes in air, the sol-gel film on the silicon was converted into Ga-Zn-O precursor serving for in-situ nanostructure growth. Finally, as-synthesized Ga-Zn-O precursor film was transferred to a resistance furnace for nitridation reaction. The reaction temperatures were fixed at 800, 850 and 900 °C and the NH_3 gas flowing rate was set at 50 sccm. To investigate the influence of growth time on the morphology evolution and composition change, time dependent experiments (30, 60 and 120 minutes) were also carried out at 800 °C.

Characterization

The morphology of the as-prepared nanorods is characterized by a Zeiss Supra 55 field-emission scanning electron microscope (FE-SEM) operating at 20 kv. The microstructure and composition of the samples are studied and analysed by using a Tecnai G2 F20 high-resolution field emission transmission electron microscope (FE-TEM) in combination with an X-ray energy dispersive spectrometer (EDS). The phase purity of $(GaN)_{1-x}(ZnO)_x$ nanorods is identified by means of an X-ray powder diffractometer (XRD, Rigaku RINT 2000) based on Cu Kα radiation. The UV-visible diffuse reflectance of spectroscopy (DRS: HITACHI U-3900) was used to analyse the overall optical properties of as-synthesized samples. The CL spectra of single $(GaN)_{1-x}(ZnO)_x$ nanorod were collected in an field emission scanning electron microscope (FE-SEM: HITACHI SU6600) equipped with CL system (HORIBA MP32). The applied voltage and beam current were set to 5 kV and 100 pA, respectively.

Acknowledgements

This work was partially supported by the Knowledge Innovation Program of Institute of Metal Research with grants No. Y2NCA111A1 and Y3NCA111A1, and the Youth Innovation Promotion Association, Chinese Academy of Sciences (Grant No.Y4NC711171). The valuable discussion with Dr. B. Yang is also greatly appreciated.

Notes and references

1. Y. Sun and Y. Xia, *Science*, 2002, **298**, 2176-2179.
2. M. N. Mankin, R. W. Day, R. Gao, Y. S. No, S. K. Kim, A. A. McClelland, D. C. Bell, H. G. Park and C. M. Lieber, *Nano Lett.*, 2015, **15**, 4776-4782.
3. X. Wang, X. Han, S. Xie, Q. Kuang, Y. Jiang, S. Zhang, X. Mu, G. Chen, Z. Xie and L. Zheng, J. *Chem.*, 2012, **18**, 2283-2289.
4. X. Y. Yu, Q. Q. Meng, T. Luo, Y. Jia, B. Sun, Q. X. Li, J. H. Liu and X. J. Huang, *Sci. Rep.*, 2013, **3**, 2886.
5. G. Liu, H. G. Yang, J. Pan, Y. Q. Yang, G. Q. Lu and H. M. Cheng, *Chem. Rev.*, 2014, **114**, 9559-9612.
6. N. Tian, Z. Y. Zhou, S. G. Sun, Y. Ding and Z. L. Wang, *Science*, 2007, **316**, 732-735.
7. S. Fan, B. AlOtaibi, S. Y. Woo, Y. Wang, G. A. Botton and Z. Mi, *Nano Lett.*, 2015, **15**, 2721-2726.
8. J. H. Zeng, B. B. Jin and Y. F. Wang, *Chem. Phys. Lett.*, 2009, **472**, 90-95.
9. F. Lin, D. Wang, Z. Jiang, Y. Ma, J. Li, R. Li and C. Li, *Energy Environ. Sci.*, 2012, **5**, 6400-6406.
10. B. Wang, S. Shen and L. Guo, *Appl. Catal. B: Environmental*, 2015, **166-167**, 320-326.
11. K. Park, J. A. Lee, H. S. Im, C. S. Jung, H. S. Kim, J. Park and C. L. Lee, *Nano Lett.*, 2014, **14**, 5912-5919.
12. J. N. Hart and N. L. Allan, *Adv. Mater.*, 2013, **25**, 2989-2993.
13. X. J. Zhuang, C. Z. Ning and A. L. Pan, *Adv. Mater.*, 2012, **24**, 13-33.
14. A. L. Pan, R. B. Liu, M. H. Sun and C. Z. Ning, *ACS Nano*, 2010, **4**, 671-680.
15. A. L. Pan, R. B. Liu, M. H. Sun and C. Z. Ning, *J. Am. Chem. Soc.*, 2009, **131**, 9502.
16. P. Guo, X. Zhuang, J. Xu, Q. Zhang, W. Hu, X. Zhu, X. Wang, Q. Wan, P. He, H. Zhou and A. Pan, *Nano Lett.*, 2013, **13**, 1251-1256.
17. K. Maeda, K. Teramura, T. Takata, M. Hara, N. Saito, K. Toda, Y. Inoue, H. Kobayashi and K. Domen, *J. Phy. Chem. B*, 2005, **109**, 20504-20510.
18. K. Maeda, K. Teramura, N. Saito, Y. Inoue and K. Domen, *J. Catal.*, 2006, **243**, 303-308.
19. C. H. Chuang, Y. G. Lu, K. Lee, J. Ciston and G. Dukovic, *J Am. Chem. Soc.*, 2015, **137**, 6452-6455.
20. K. Maeda, K. Teramura, D. Lu, T. Takata, N. Saito, Y. Inoue and K. Domen, *Nature*, 2006, **440**, 295.
21. K. Lee, B. M. Tienes, M. B. Wilker, K. J. Schnitzenbaumer and G. Dukovic, *Nano Lett.*, 2012, **12**, 3268-3272.
22. K. Maeda and K. Domen, *Chem. Mater.*, 2010, **22**, 612-623.
23. W. Q. Han, Z. Liu and H. G. Yu, *Appl. Phys. Lett.*, 2010, **96**, 183112.
24. K. Maeda, T. Takata, M. Hara, N. Saito, Y. Inoue, H. Kobayashi and K. Domen, *J. Am. Chem. Soc.*, 2005, **127**, 8286-8287.
25. K. Teramura, K. Maeda, T. Saito, T. Takata, N. Saito, Y. Inoue and K. Domen, *J. Phys. Chem. B*, 2005, **109**, 21915-21921.
26. K. Maeda, K. Teramura, D. Lu, N. Saito, Y. Inoue and K. Domen, *J. Phys. Chem. C*, 2007, **111**, 7554-7560.
27. K. Maeda, K. Teramura and K. Domen, *J. Catal.*, 2008, **254**, 198-204.
28. Y. Li, L. Zhu, Y. Yang, H. Song, Z. Lou, Y. Guo and Z. Ye, *Small*, 2015, **11**, 871-876.
29. C. Sun, L. M. Liu, A. Selloni, G. Q. Lu and S. C. Smith, *J. Mater. Chem.*, 2010, **20**, 10319.
30. X. G. Han, X. Wang, S. F. Xie, Q. Kuang, J. J. Ouyang, Z. X. Xie and L. S. Zheng, *RSC Adv.*, 2012, **2**, 3251-3253.
31. C. Liu, X. G. Han, S. F. Xie, Q. Kuang, X. Wang, M. S. Jin, Z. X. Xie and L. S. Zheng, *Chem. Asian J.*, 2013, **8**, 282-289.
32. B. Liu, Y. Bando, L. Liu, J. Zhao, M. Masanori, X. Jiang and D. Golberg, *Nano Lett.*, 2013, **13**, 85-90.
33. W. Yang, B. Liu, B. Yang, J. Wang, T. Sekiguchi, S. Thorsten and X. Jiang, *Adv. Funct. Mater.*, 2015, **25**, 2543-2551.
34. F. Yuan, B. Liu, Z. Wang, B. Yang, Y. Yin, B. Dierre, T. Sekiguchi, G. Zhang and X. Jiang, *ACS Appl. Mater. & Inter.*, 2013, **5**, 12066-12072.
35. Y. Yin, R. M. Rioux, C. K. Erdonmez, S. Hughes, G. A. Somorjai and A. P. Alivisatos, *Science*, 2004, **304**, 711-714.
36. C. Hahn, M. A. Fardy, C. Nguyen, M. Natera-Comte, S. C. Andrews and P. Yang, *Isr. J. Chem.*, 2012, **52**, 1111-1117.
37. Z. Y. Jiang, Q. Kuang, Z. X. Xie and L. S. Zheng, *Adv. Funct. Mater.*, 2010, **20**, 3634-3645.
38. G. Liu, H. G. Yang, X. Wang, L. Cheng, H. Lu, L. Wang, G. Q. Lu and H. M. Cheng, *J. Phys. Chem. C*, 2009, **113**, 21784-21788.
39. J. Yan, X. Fang, L. Zhang, Y. Bando, U. K. Gautam, B. Dierre, T. Sekiguchi and D. Golberg, *Nano Lett.*, 2008, **8**, 2794-2799.
40. P. W. Voorhees, *J. Stat. Phys.*, 1985, **38**, 231-252.
41. J. W. Gibbs, *In Collected Works*, ed. G. C. Longmans, New York, 1928.
42. L. L. Jensen, J. T. Muckerman and M. D. Newton, *J. Phys. Chem. C*, 2008, **112**, 3439-3446.